ARL-TR-9832 ● Nov 2023

Evaluation of Additively Manufactured Ultrahard Steels

by Vincent Hammond, Taylor Cain, Jonathan Ligda, Paul Moy, Nikhil Murthy, Brian Powers, Timothy Walter, Monica Ferrera, Caleb McCoy, and Diana Berman

NOTICES

Disclaimers

The findings in this report are not to be construed as an official Department of the Army position unless so designated by other authorized documents.

Citation of manufacturer's or trade names does not constitute an official endorsement or approval of the use thereof.

Destroy this report when it is no longer needed. Do not return it to the originator.

ARL-TR-9832 ● Nov 2023

Evaluation of Additively Manufactured Ultrahard Steels

Vincent Hammond, Taylor Cain, Jonathan Ligda, Paul Moy, Nikhil Murthy, Brian Powers, Timothy Walter, and Monica Ferrera
DEVCOM Army Research Laboratory

Caleb McCoy and Diana Berman
University of North Texas

REPORT DOCUMENTATION PAGE

1. REPORT DATE	2. REPORT TYPE	3. DATES COVERED	
		START DATE	END DATE
November 2023	Technical Report	1 September 2021	30 September 2022

4. TITLE AND SUBTITLE
Evaluation of Additively Manufactured Ultrahard Steels

5a. CONTRACT NUMBER	5b. GRANT NUMBER	5c. PROGRAM ELEMENT NUMBER
5d. PROJECT NUMBER	**5e. TASK NUMBER**	**5f. WORK UNIT NUMBER**

6. AUTHOR(S)
Vincent Hammond, Taylor Cain, Jonathan Ligda, Paul Moy, Nikhil Murthy, Brian Powers, Timothy Walter, Monica Ferrera, Caleb McCoy, and Diana Berman

7. PERFORMING ORGANIZATION NAME(S) AND ADDRESS(ES)
DEVCOM Army Research Laboratory
ATTN: FCDD-RLA-MF
Aberdeen Proving Ground, MD 21005

8. PERFORMING ORGANIZATION REPORT NUMBER
ARL-TR-9832

9. SPONSORING/MONITORING AGENCY NAME(S) AND ADDRESS(ES)	10. SPONSOR/MONITOR'S ACRONYM(S)	11. SPONSOR/MONITOR'S REPORT NUMBER(S)

12. DISTRIBUTION/AVAILABILITY STATEMENT
DISTRIBUTION STATEMENT A. Approved for public release: distribution unlimited.

13. SUPPLEMENTARY NOTES
ORCID IDs: Vincent Hammond, 0000-0002-9561-6216; Taylor Cain, 0000-0002-6621-914X; Jonathan Ligda, 0000-0003-3539-8867; Brian Powers, 0000-0002-9579-1006; Timothy Walter, 0000-0002-1786-3668

14. ABSTRACT
Recent advances in both alloy development and additive manufacturing have enabled the production of ultrahigh-strength steels in near-net shape parts. Compared with traditional manufacturing methods, such parts would result in significant savings in both time and overall cost due to faster production rates with lower machining requirements and/or material waste. However, before widespread acceptance of such components, these new alloys and production methods must be evaluated to ensure the required properties and performance are achieved. Toward this goal, a series of test samples produced from three different alloys via additive manufacturing were acquired from a Swedish company and evaluated over a range of physical and mechanical properties. Key findings from this study indicated that the sizeable amount of carbides in these alloys resulted in their ultrahigh strengths and hardness but at the cost of reduced tensile ductility. As a result, the alloys were deemed to be best suited for use in applications requiring high wear resistance. Their performance in this area combined with the potential to redesign existing parts by leveraging capabilities offered by additive manufacturing provides an opportunity to develop a new series of high-performance components at lower cost relative to existing alloys.

15. SUBJECT TERMS
Sciences of Extreme Materials, additive manufacturing, steels, tensile response, fatigue performance, wear testing, corrosion

16. SECURITY CLASSIFICATION OF:			17. LIMITATION OF ABSTRACT	18. NUMBER OF PAGES
a. REPORT	b. ABSTRACT	C. THIS PAGE		
UNCLASSIFIED	UNCLASSIFIED	UNCLASSIFIED	UU	31

19a. NAME OF RESPONSIBLE PERSON	19b. PHONE NUMBER *(Include area code)*
Vincent Hammond	(410) 278-2752

STANDARD FORM 298 (REV. 5/2020)
Prescribed by ANSI Std. Z39.18

Contents

List of Figures

List of Tables

Acknowledgments

The authors would like to extend their acknowledgment and appreciation for the funding of this effort by the Office of the Secretary of Defense under the Foreign Technology Assessment Support Program.

1. Introduction

Ultrahigh-strength steels are traditionally defined as those steels with a minimum yield strength of approximately 1380 MPa. Notable examples of steels in this category include AISI 4130, AISI 4140, and AISI 4340. In many cases, maximizing the performance of these alloys requires a rather complex approach that involves a series of tempering, annealing, or stress-relieving treatments. As a result, they are produced using a variety of traditional processing methods such as casting, rolling, extrusion, or forging. These traditional methods—combined with the ultrahigh strength of the steels—often meant that the production of complex, near-net shape parts of high quality was quite difficult. In addition, these production methods often entailed repetitive treatments or long production cycles, both of which resulted in elevated production costs.

Additive manufacturing ([AM] also known as 3D printing) has recently been recognized as a manufacturing method that enables the production of near-net shape parts. In these methods, a complex part is iteratively built in a layer-by-layer process that involves powder deposition followed by selective melting/sintering of the powder to form the part. With the continued development of processing lasers, it is now possible to form fully dense components from a wide range of metals powders, including refractory alloys, steels, and other high-temperature alloys. Furthermore, parts produced by 3D printing often require less finishing work, which results in faster production cycles and potentially significant cost savings. Furthermore, the metal powder not incorporated into the part is often reclaimed and, after a cleaning protocol that involves sieving and removal of agglomerates, can be used in the next build operation. This ability to "reuse" the metal powder also offers appreciable cost savings relative to the scrap waste produced by the casting and machining of larger metal blocks to final parts.

Although there is great potential associated with the AM of ultrahigh-strength steel components, there are also significant challenges that must be addressed, typically on an alloy-by-alloy basis. For example, many of these steels have highly complex compositions (e.g., multiple alloying elements) that are intended to form a desired range of strengthening precipitates or phases. Due to their broad compositional range, it can be quite challenging to understand, predict, and/or control the interaction between the laser energy and metal powder during the printing process. As a result, it often requires a prolonged investigation and process optimization routine to achieve the desired microstructure in the final, printed component. Other factors that must also be addressed to achieve high-quality parts are the removal of property dependence on build direction, high residual stresses, and undesired microstructural features such as pores and/or cracks. From even this brief

consideration, it is clear that the production of high-quality parts using AM is not a trivial process, but it typically involves many hours of part building and evaluation to develop the desired process parameters.

As a result, an effort was undertaken to acquire and evaluate a series of ultrahigh-strength steels produced by VBN Components (Uppsala, Sweden) using AM. In particular, VBN has successfully developed a series of ultrahard steels that have demonstrated extreme wear and thermal resistance that could potentially offer improved performance and component lifetime. The superior performance of these alloys was achieved through a combination of compositional designs as well as optimization of annealing treatments. Furthermore, VBN has developed proprietary AM-based processing routines that enable the production of near-net shape components from the entire range of alloys.

Various sample types produced from three different alloys were procured from VBN Components in the fully annealed and surface ground conditions (e.g., ready to test conditions). This report provides a summary of the key findings from this evaluation effort as well as potential areas for further study.

2. Materials

Three alloys were ordered from VBN to evaluate the material for a range of potential applications. In general, the microstructure of the alloys consists of a fine-grained Fe matrix with a dispersion of small carbides. The amount and type of carbides is dependent on alloy chemistry (Table 1). The first alloy, designated Vibenite 150, is promoted as having the highest level of toughness and fatigue resistance among the Vibenite alloy family. The alloy has a hardness range of 58–64 Rockwell C (HRC). The second alloy, Vibenite 280, displays exceptional wear and heat resistance and as such is suitable for cutting tool-based applications. Hardness for this alloy ranges from 63 to 70 HRC. The third alloy, Vibenite 350, is a stainless steel that is well suited for high-wear applications in which corrosion resistance is also a consideration. Hardness of this alloy is approximately 60 HRC.

Table 1 Composition (weight percent) of the three Vibenite alloys examined in this study

Alloy designation	C	Cr	Mo	W	Co	V	Fe
150	1.5	4.0	2.5	2.5	…	4.0	Bal
280	2.3	4.2	7.0	6.5	10.5	6.5	Bal
350	1.9	20.0	1.0	…	…	4.0	Bal

Depending on the desired test, multiple sample geometries and quantities were received from VBN. Details for both the test and sample geometry are provided in Table 2. Furthermore, samples were ordered such that they were delivered in their final machining state—that is, no further grinding or polishing were required before they could be tested. Upon receipt, however, issues were noticed with some of the samples. First, samples provided for use in the split Hopkinson bar tests were too large and were subsequently machined to be 6-mm-diameter by 6-mm-long cylinders. Second, and more significantly, the majority of the Alloy 150 and Alloy 350 cylinders intended for the tensile and fatigue testing had been improperly machined. Rather than having the desired geometry (per ASTM E466[1]) for a reduced gage section of 5-mm diameter and 15-mm gage length, the improperly machined samples had a reduced gage length of 50 mm (Fig. 1). Alloy 280 samples were provided in the proper dimensions, whereas Alloy 150 and 350 samples were provided in the extended gage length geometry.

Table 2 Sample geometry and quantities for indicated test methods

Suggested test	Tensile test
Sample dimension	Diam 10 mm, L = 140 mm
Sample qty	10 pcs
Suggested test	Charpy impact test
Sample dimension	55 × 10 × 7 mm
Sample qty	20 pcs
Suggested test	Uniaxial fatigue test
Sample dimension	Diam 10 mm, L = 140 mm
Sample qty	20 pcs
Suggested test	Corrosion tests
Sample dimension	Diam 25 mm, H = 5 mm
Sample qty	2 pcs
Suggested test	Split Hopkinson bar tests
Sample dimension	20 × 20 × 20 mm
Sample qty	5 pcs
Suggested test	Wear test
Sample dimension	Diam 50 mm, H = 6.35 mm, Diam 25 mm, H = 6.35 mm, Diam 9.53 mm, H = 3.18 mm
Sample qty	5, 15, and 5 pcs, respectively

Note: Diam, diameter; H, height; L, length; pcs, pieces; qty, quantity.

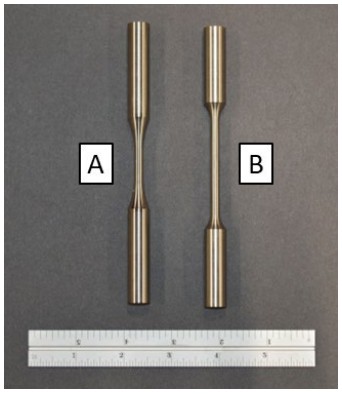

Fig. 1 Vibenite tension test specimens. Sample A is the desired geometry whereas sample B shows the extended gage region.

3. Results

3.1 Density/Hardness

Before the initiation of the test program, all samples were visually inspected and found to be free of any noticeable surface defects upon arrival. Next, five small cylinders cut from the oversized Hopkinson bar samples were used to measure average density using the Archimedes' method. As seen in Table 3, the samples had a theoretical density on the order of 97%–98%. The presence of some fine porosity was confirmed in subsequent CT scans on selected samples. A series of hardness measurements were then conducted using both Rockwell C and Vickers hardness. In general, the measured values are in good agreement with the targeted values provided by VBN (Table 4).

Table 3 Density measurements obtained from representative samples of each alloy

Sample	Average density and deviation (g/cc)	Theoretical density (%)
Alloy 150	7.669 ± .0285	98.32
Alloy 280	7.776 ± .0357	98.43
Alloy 350	7.485 ± .0146	97.21

Table 4 Hardness values for each alloy

Sample	Rockwell C/Vickers hardness	VBN target (Rockwell C)
Alloy 150	59.3/741.5	58
Alloy 280	69.1/1059.5	70
Alloy 350	55.3/664.2	60

Finally, five samples were evaluated using room temperature Charpy impact testing to gain insight into the toughness of the alloys under high-strain-rate conditions. Due to their high hardness, the samples were in the form of rectangular bars (e.g., without notches). Two samples from the Alloy 150 and Alloy 280 results were discarded due to extremely low energy values. Visual examination of these samples revealed large precipitates or porosity that were judged to be the cause of the abnormally poor performance. The results confirm that Alloy 150 has the highest toughness of the three alloys (Table 5).

Table 5 Charpy impact strength for each alloy

Sample	Charpy impact strength (J)
Alloy 150	27.10 ± 7.74
Alloy 280	10.43 ± 1.11
Alloy 350	10.12 ± 1.24

3.2 Microstructural Evaluation

Representative samples of each alloy were prepared and then examined using scanning electron microscopy. In particular, high-resolution images as well as electron back-scatter diffraction (EBSD) plots (Figs. 2–4) were collected in order to understand microstructural details that would govern the mechanical response of the alloys. The images clearly show the presence of small carbide(s) in a ferrite matrix, as mentioned in Section 2.

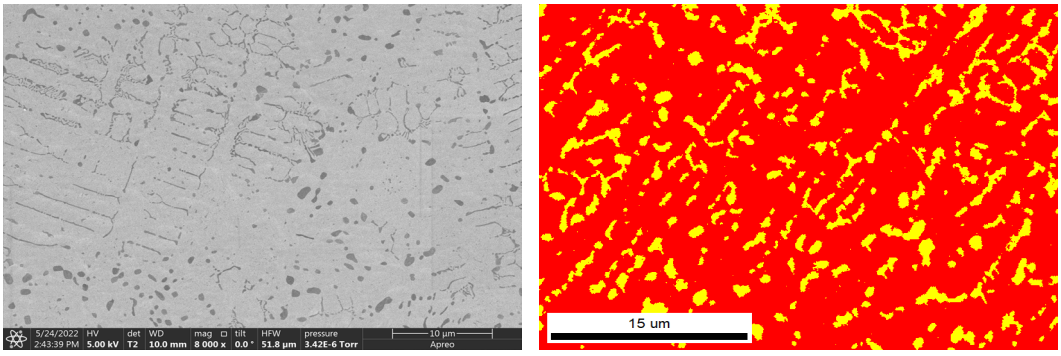

Fig. 2 Representative image and EBSD map of Alloy 150. In the EBSD map, red is the ferrite matrix and yellow is the vanadium carbide precipitates.

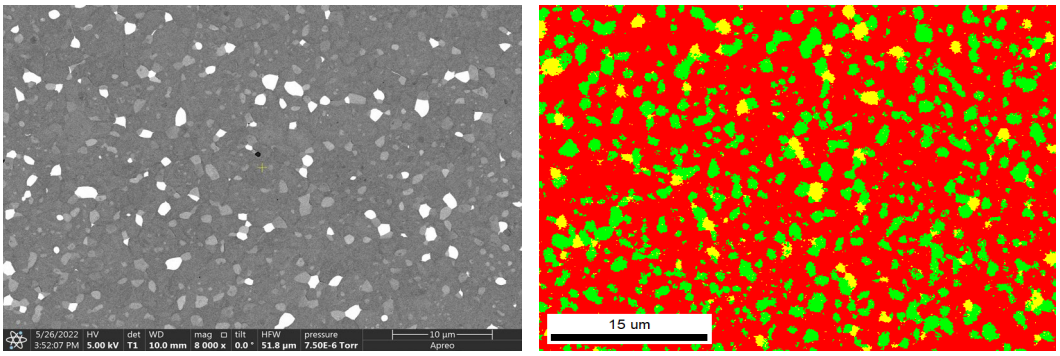

Fig. 3 Representative image and EBSD map of Alloy 280. In the EBSD map, red is the ferrite matrix, green is the vanadium carbide precipitates, and yellow is the tungsten carbide precipitates.

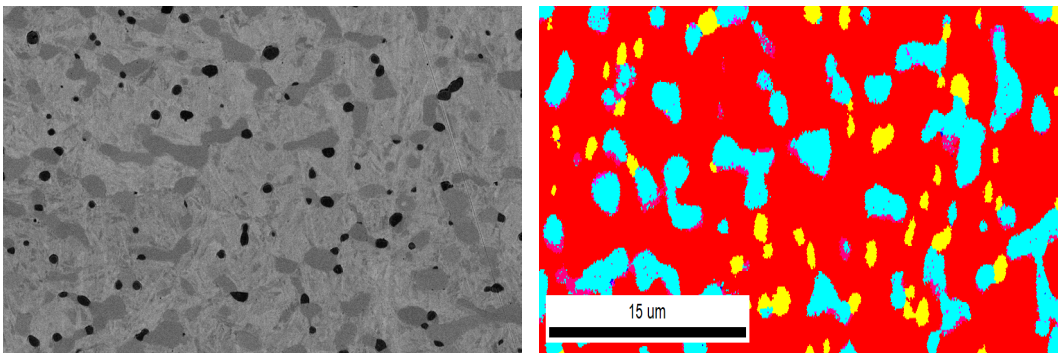

Fig. 4 Representative image and EBSD map of Alloy 350. In the EBSD map, red is the ferrite matrix, yellow is the vanadium carbide precipitates, and blue is a complex chromium carbide (Cr_7C_3) precipitate.

In addition, grain-size measurements were also performed for each alloy matrix as well as carbides present in the alloys. Results from this analysis indicate that the majority of ferrite grains are smaller than 1 μm, with the largest grain size observed in the alloys being on the order of 3 μm (Fig. 5). This extremely fine grain size after a prolonged annealing treatment is attributed to the widespread presence of carbides, which prevent significant grain growth during the high temperature heat treatments. Similarly, size analysis of the carbides present in the alloys indicated that a majority of the vanadium carbide and tungsten carbide precipitates were smaller than 1 μm, whereas the majority of the Cr_7C_3 precipitates were between 1 and 3 μm in size.

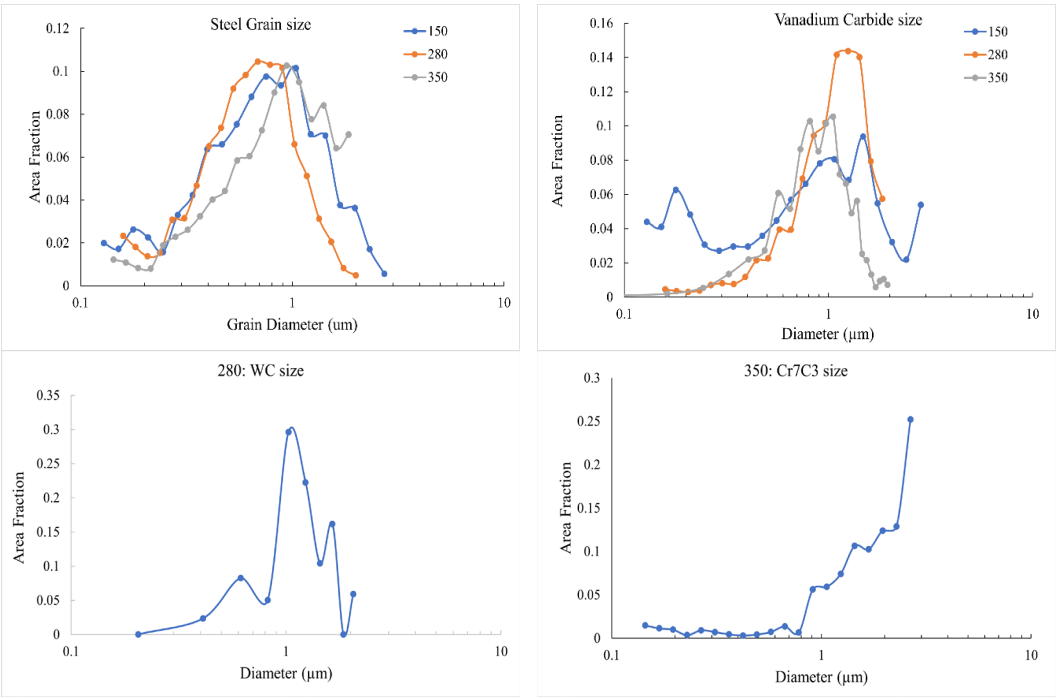

Fig. 5 Ferrite grain size and carbide size analysis for the three alloys (WC = tungsten carbide)

3.3 Mechanical Testing: Tension

Uniaxial tensile tests were performed under quasi-static loading rates on four samples from each alloy. VBN provided samples in two different geometries as discussed previously and pictured in Fig. 1. Alloy 280 was machined to "A", whereas both Alloy 150 and 350 conform to "B". Experiments were conducted on an MTS 809 servo-hydraulic load frame at a displacement control rate that equates to strain rate of approximately 0.001/s. Hydraulic pressurized grips with appropriate inserts were used to accommodate the 12-mm-diameter smooth grip region of the cylindrical tensile samples. These inserts have a carbide grit textured surface to ensure slipping does not occur during testing for high-strength materials. Strains were determined from the actuator displacement in combination with machine compliance correction.

Test results from samples that failed in the gage section were deemed valid and subsequently included in the final tabulation for the stress-strain results. Sample T03 in the Alloy 350 set was discarded because it failed inside the grip section. The resulting curves and material properties are provided in Fig. 6 and Table 6, respectively. Alloy 150 exhibited the highest strength among the three VBN steels and show evidence of yielding (~2,041 MPa) prior to failure. Alloy 350 has a minimal amount of strain after yielding, whereas Alloy 280 essentially displayed a linear elastic response up to a rupture strain of approximately 0.017. As a note,

measured deformation may not be the true representation of the materials' failure strains for the Vibenite alloys because axial strains were determined from machine displacement. Nevertheless, these results provide an approximation for the mechanical response for "as-received" steels from VBN. For comparison, tensile strength data from VBN for Alloy 150 is approximately 2,393 MPa and 2,414 MPa for AM printed in the horizontal and vertical orientations, respectively. The average strength is 2,230 MPa from our results. At the time of the publication of this report, we had not received any VBN-produced tensile data for Alloys 280 and 350.

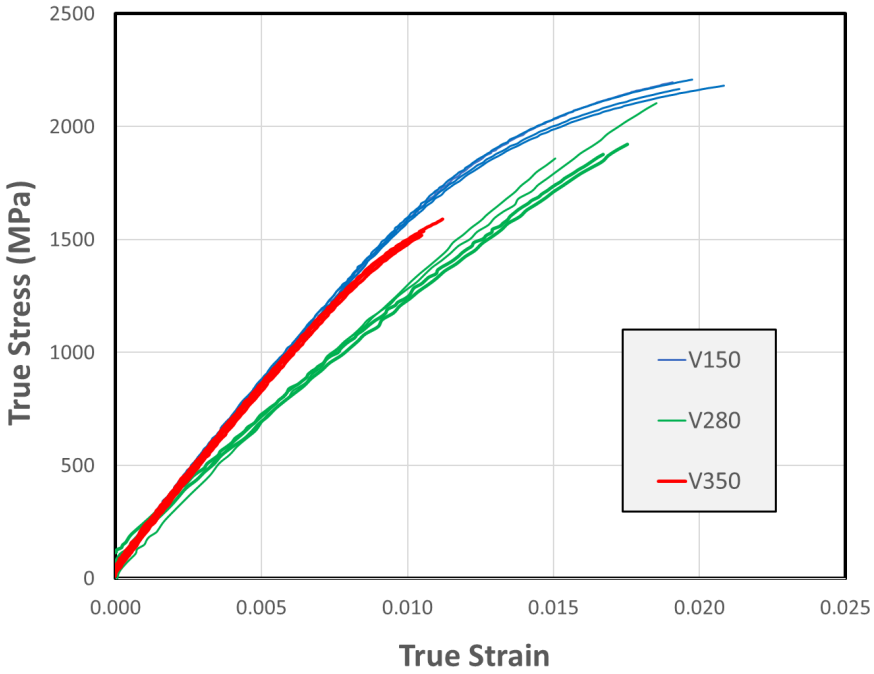

Fig. 6 Tensile stress-strain curves for Vibenite alloys

Table 6 Tensile properties obtained from the alloys

Sample	Ultimate tensile strength (MPa)	Failure strain	Elastic modulus (GPa)	Yield strength (MPa)
Alloy 150	2230.93 ± 18.65	0.0195 ± 0.0008	164.38 ± 1.72	2041.03 ± 35.59
Alloy 280	1566.02 ± 38.76	0.0107 ± 0.0004	160.75 ± 0.94	…
Alloy 350	1947.58 ± 119.43	0.0168 ± 0.0014	125.61 ± 6.82	…

3.4 Mechanical Testing: Tension-Tension Fatigue

Based on the observed tensile response, it was decided that fatigue tests would only be performed on the Alloy 150 samples because this alloy displayed the highest failure strain as well as best overall toughness. A series of tensile fatigue tests were performed using a fatigue stress ratio, R, of 0.1 at a frequency of 20 Hz on servo-hydraulic Instron 1331 test frame. An applied load from the range of 30% to 60%

of the average ultimate tensile stress was used for each cyclic test. The resulting stress-lifetime (cycles to failure) curve is shown in Fig. 7. Assessment is inconclusive on whether the specimen geometry is playing a role to the higher-than-normal scatter in the stress amplitude–cycles to failure (S-N) data or whether this behavior is due to other contributing factors (such as porosity and/or cracks) in the material.

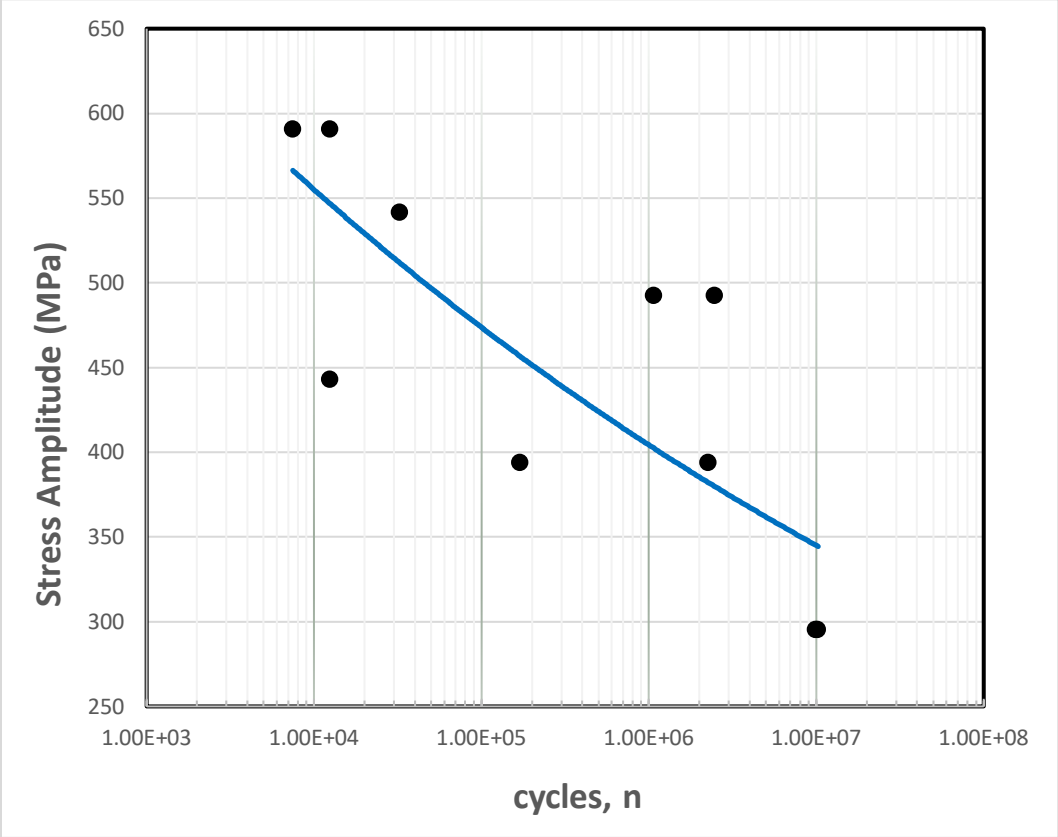

Fig. 7 S-N data for Vibenite 150

3.5 Mechanical Testing: Quasi-static and High-Rate Compression

A set of six right-cylindrical compression samples were fabricated from each VBN alloys. The length-to-diameter ratio is 1:1. Two quasi-static compression tests for each alloy were conducted on an Instron model 8595 electro-mechanical material testing load system. A 5.08-cm-diameter sub-press fixture from Wyoming Test Fixture was used to assist in sample alignment and also provides pressure distribution across the 15.24-cm-diameter Instron loading platen. Due to the hardness of the Vibenite alloys, sacrificial tungsten carbide platens were used to avoid damaging/pitting of the OEM test fixture when sample failure occurred. If necessary, the carbide platens were replaced between tests. Displacement

measurements were recorded from the machine crosshead travel, which was set at a rate of 0.006 mm/s. This equates to a strain rate of approximately 0.001/s. System compliance was determined to further correct the displacement data because this was used to calculate the axial strains. Figure 8 shows the compression testing setup with the compression sample between two carbide platens.

Fig. 8 Quasi-static compression testing setup

High-strain-rate compression experiments were conducted on a 38.1-mm (1.5 inches)-diameter Kolsky bar from REL, Inc. (Calumet, MI). Both the incident and transmitted bars are approximately 3.6 m (144 inches) in length and are made from Maraging 300 steel. Thin copper disks were used as pulse shapers to reduce the high frequency component of the incident stress wave and to increase the rise time of the initial loading pulse imparted when the striker impacts the incident bar. This technique allows the test sample to reach dynamic stress equilibrium at each of the bar/specimen interfaces and a nearly constant strain rate. This is particularly important for brittle materials. Thorough details on the fundamental operations and data interpretation for Kolsky bar experiments are described in Chen and Song.[2] Similar to the quasi-static experiments, carbide platens were used to protect the bar ends and, if necessary, they were replaced between tests. Figures 9a–9c are the compressive stress-strain results for each of the Vibenite alloys. The solid lines represent the two quasi-static tests, and the dashed lines are the high-rate strain rates at approximately 1000/s. Table 7 provides a comprehensive summary for the performance of all alloys at both strain rates.

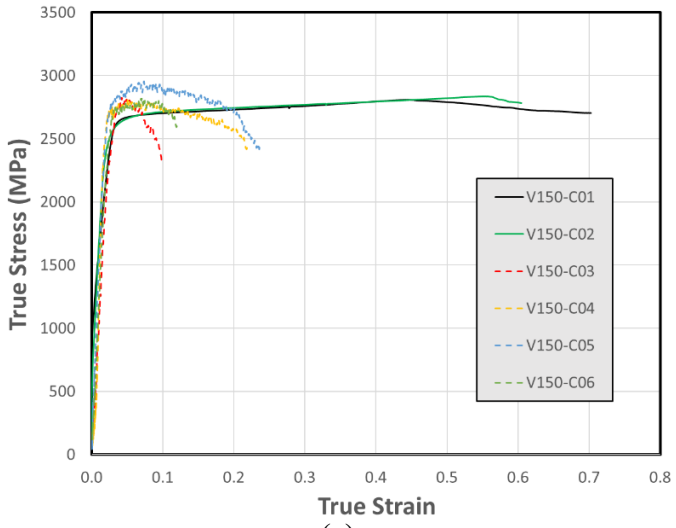

(a)

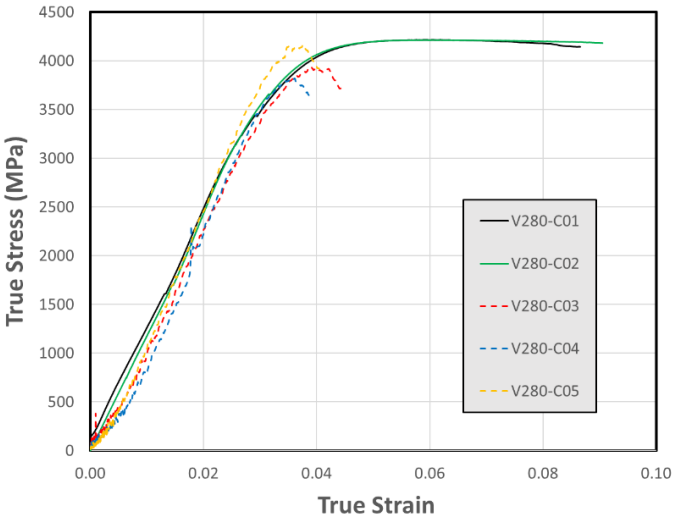

(b)

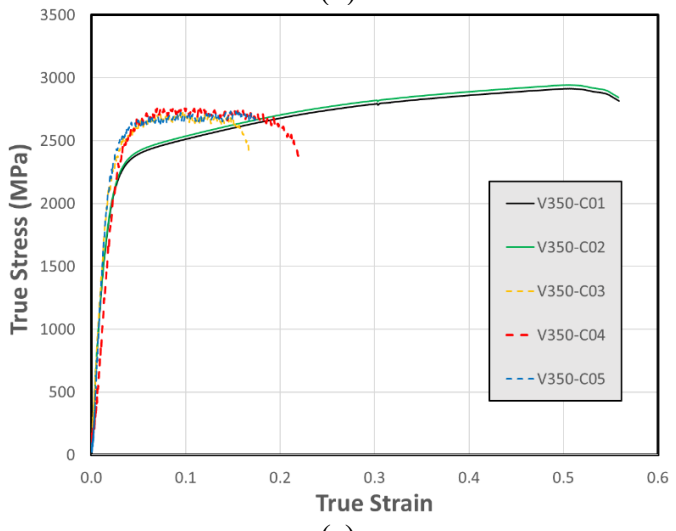

(c)

Fig. 9 (a–c) Compression stress-strain results at quasi-static and high rates

Table 7 Summary of compression results

Sample	Compression strength (MPa)	Strain at maximum stress	Strain rate (1/s)
V150-C01	2808.70	0.7608	
V150-C02	2836.36	0.6047	~0.001
Avg ± SD	2822.54 ± 19.57	0.6827 ± 0.1104	
V150-C03	2826.66	0.1135	
V150-C04	2805.94	0.2522	
V150-C05	2955.32	0.2366	~1000
V150-C06	2829.65	0.1414	
Avg ± SD	2854.89 ± 67.84	0.1859 ± 0.0688	
V280-C01	4214.94	0.0866	
V280-C02	4213.77	0.0905	~0.001
Avg ± SD	4214.35 ± 0.82	0.0885 ± 0.0028	
V280-C03	3936.56	0.0498	
V280-C04	3819.69	0.0388	~1000
V280-C05	4161.42	0.0405	
Avg ± SD	3972.55 ± 173.69	0.0430 ± 0.0059	
V350-C01	2914.41	0.5588	
V350-C02	2943.44	0.5582	~0.001
Avg ± SD	2928.92 ± 20.53	0.5585 ± 0.0004	
V350-C03	2735.72	0.1666	
V350-C04	2774.27	0.2212	~1000
V350-C05	2734.40	0.1750	
Avg ± SD	2748.13 ± 22.65	0.1876 ± 0.0294	

Note: Avg, average; SD, standard deviation.

First and foremost, the compression response between the static and dynamic results is drastically different. In all incidences, the peak strains trend higher at the low strain rates tests, whereas they were significantly reduced to more than 50% at high rates for each of the Vibenite alloys. At low rates, Alloy 150 exhibits a significant amount of plastic stress after the yield, whereas Alloy 350 tends to strain harden after yielding up to approximately 55% strain. Alloys 150 and 350 indicate some rate sensitivity response because the flow stresses increase slightly at strain rates from 10^{-3}/s to approximately 1,000/s.

It is interesting to note that Alloy 280, which has almost no ductility under tension, does yield during quasi-static loading prior to failing just below 10% strain. Although it trends like most brittle materials, this alloy is not strain-rate sensitive; nevertheless, it has the overall highest compressive strength in comparison to the other two alloys in this study.

Figure 10a shows a photo of quasi-static tested Alloy 150, which has been strained to more than 50% while remaining intact. Figures 10b and 10c show the photos of

the recovered fragments from Alloys 150 and 280, respectively, from compression tests at high loading rate. Both Alloy 150 and Alloy 350 (data not shown) break up in larger and recognizable segments, whereas Alloy 280 practically fractures into numerous individual granules.

(a) (b) (c)

Fig. 10 Recovered samples of Alloy 150 after (a) quasi-static and (b) high-rate compression testing as well as Alloy 280 fragments after high-rate compression testing (c)

3.6 Computed Tomography

To elucidate the mechanical testing as to why the tensile strength seemingly underperformed per VBN's specifications, a CT scan was completed from the half section of the tested Alloy 280 tension sample. Figure 11 shows a series of slices of the cross-sectional area. An examination of the CT slices indicates that voids (i.e., dark areas) are apparent throughout the gage length and range in size from a few microns up to approximately 50 μm. While under tensile stresses, the flaws can act as crack initiation leading to complete specimen failure. In contrast, however, the voids do not greatly affect the quasi-static compression for each of the Vibenite alloys.

3.7 Wear

A series of experiments were conducted on the three alloys to evaluate the wear characteristics in a fuel-lubricated environment. In addition, AISI 52100 (a common bearing steel) specimens hardened to approximately 800 HV were included as a reference material. The materials were subjected to three types of experiments and the details shown in Table 8. In all experiments, the flat surface of the cylindrical specimens was brought into contact with a spherical counterbody while submerged in a lubricant bath. A constant normal force was applied as the two bodies were brought into reciprocating motion at a constant frequency and

stroke length for a period of 20 min. Frictional force during the experiment was measured using a tribometer. Once the test was completed, the wear of the specimens was determined using optical profilometry. The experiments were repeated three times each for four different lubricants (decane, dodecane, ethanol, and F-24 Jet fuel).

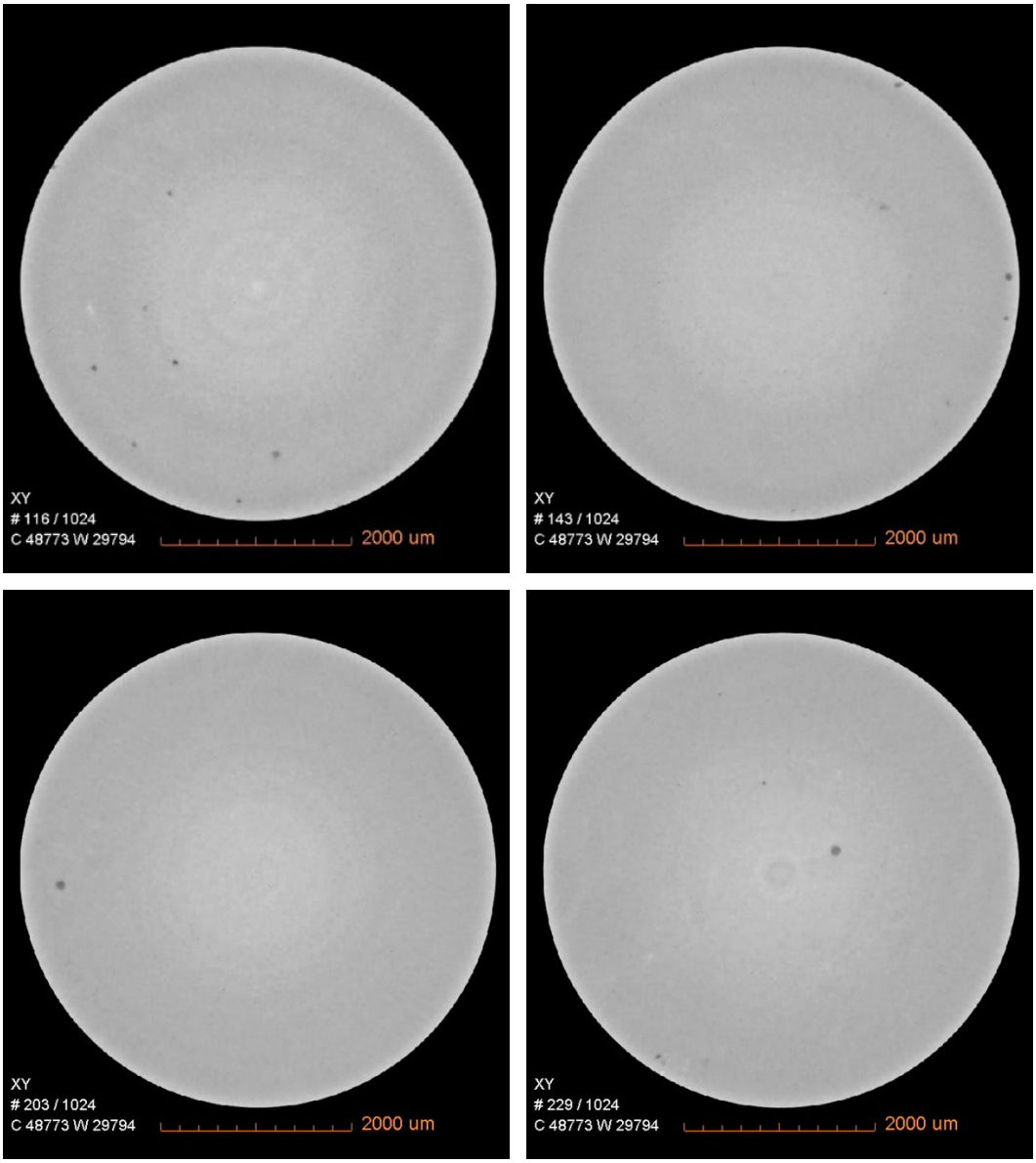

Fig. 11 CT slices for Alloy 280

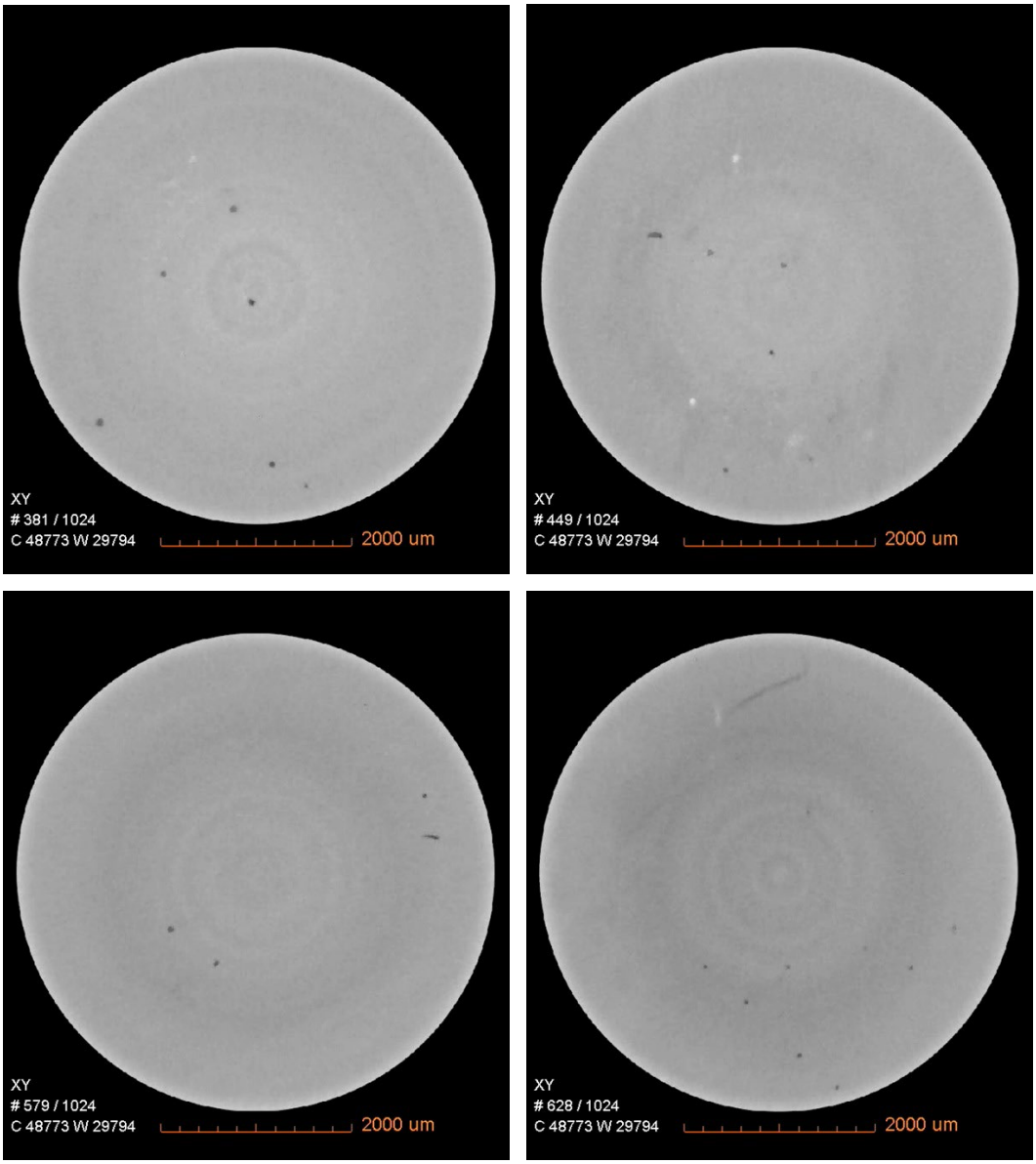

Fig. 11 CT slices for Alloy 280 (continued)

Table 8 Experimental parameters for the three wear experiments

Experimental parameters	Experiment 1	Experiment 2	Experiment 3
Specimens	AISI 52100, Vibenite 150, Vibenite 280, Vibenite 350		Vibenite 150, Vibenite 280, Vibenite 350
Surface finish	Mirror polish	Mirror polish	Ground surface Ra ~200 nm
Lubricant	Decane, dodecane, ethanol, F-24 Jet fuel		
Counterbody material	Alumina	Steel	Steel
Counterbody diameter	10 mm	10 mm	6 mm
Reciprocating frequency	20 Hz	20 Hz	20 Hz
Stroke length	10 mm	10 mm	10 mm
Normal force	10 N	10 N	N
Hertzian contact stress	~1,200 N	~1,000 N	~1,000 N
Duration	20 min	20 min	20 min
Test environment	Ambient air	Ambient air	Ambient air
Temperature	40 °C	40 °C	40 °C
Instrument (tribometer)	Phoenix TE-77	Phoenix TE-77	CETR UMT-3

Wear Experiment 1 shows the wear of the polished metal alloys against an alumina ball. The average coefficient of friction and normalized wear rates are shown in Fig. 12. The coefficient of friction was similar for all alloys to that of AISI 52100. However, the wear was much lower for all alloys than the AISI 52100.

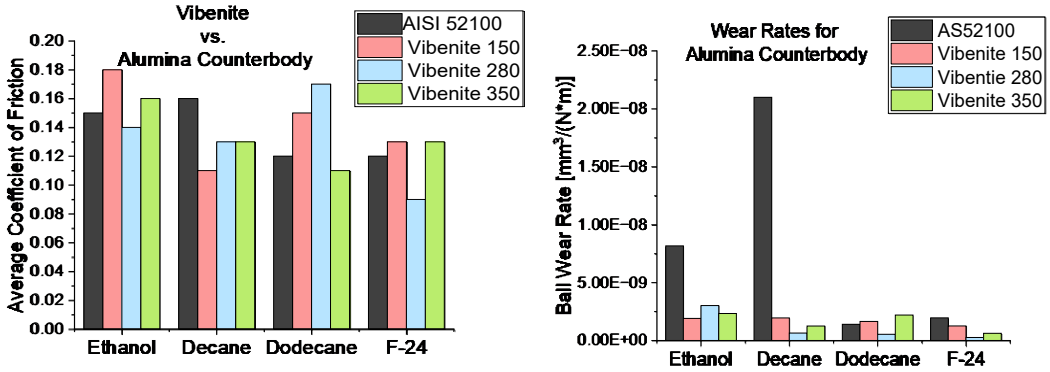

Fig. 12 Coefficient of friction (left) and normalized wear rate (right) for polished metal alloys against alumina counterbody

Wear Experiment 2 shows the wear of the polished metal alloys against an AISI 52100 ball. The average coefficient of friction and normalized wear rates are shown in Fig. 13. The results indicate a lower coefficient of friction for all the alloys compared to AISI 52100 except ethanol, which is the only non-alkane-based fuel. Although the wear behavior is much more scattered, the alloys tend to have lower wear than the AISI 52100.

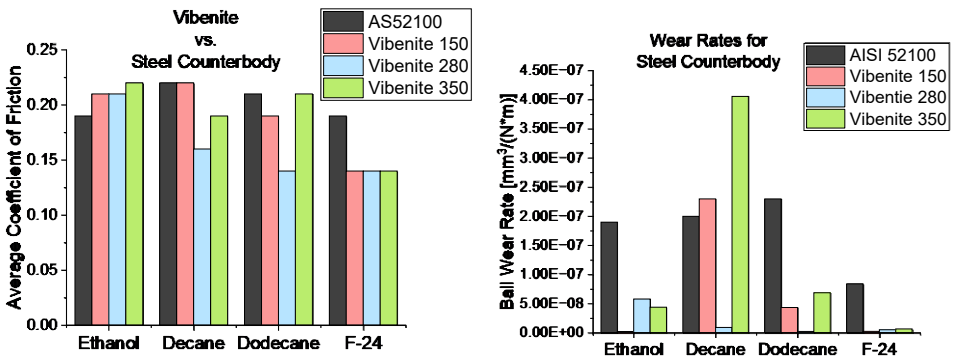

Fig. 13 Coefficient of friction (left) and normalized wear rate (right) for polished metal alloys against AISI 52100 counterbody

Wear Experiment 3 shows the wear of the surface ground metal alloys against an AISI 52100 ball. The contact in this experiment is most representative of a fuel-lubricated system. The wear became very difficult to measure due to the low wear compared to the large variation in surface topography from the rough surface. An AISI 52100 baseline was not measured. Thus, ball wear scar diameter was used as an approximation instead of the normalized wear rate. The average coefficient of friction and ball wear scar diameters are shown in Fig. 14.

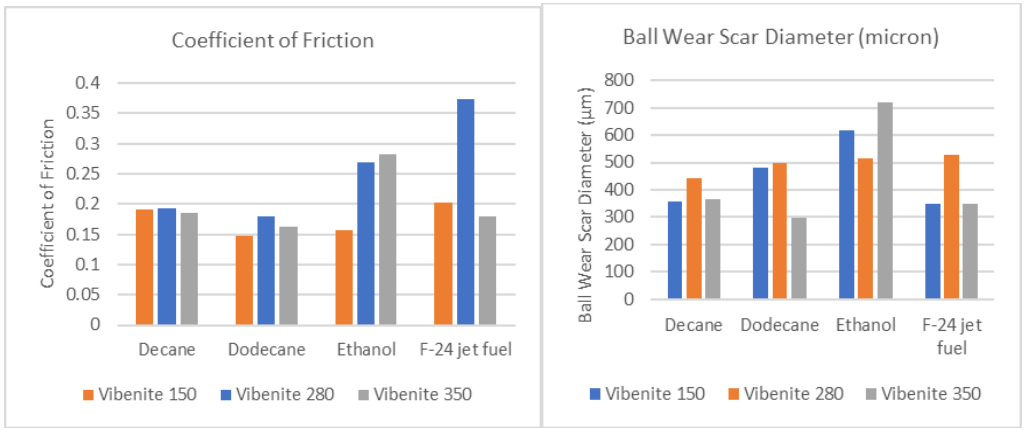

Fig. 14 Coefficient of friction (left) and normalized wear rate (right) for surface ground metal alloys against AISI 52100 counterbody

The overall tribological performance of the Vibenite alloys was comparable to the AISI 52100 alloy. Vibenite 280 had the highest hardness and best wear characteristics of all the alloys. It is significant for additively manufacture material to perform similarly to wrought alloy. Finally, it seems that surface chemistry may have had a significant effect on the wear for the Vibenite 280 and 350 Alloys.

3.8 Corrosion

All electrochemical testing was performed with a BioLogic VMP-300 potentiostat and a three-electrode flat cell comprising a working electrode, platinum mesh counter electrode, saturated Ag/AgCl reference electrode, and Teflon knife edge O-ring for the working electrode giving an exposed area of 1 cm^2. Each alloy was allowed to stabilize at their open circuit potential (OCP) for 4 h before any external polarization in quiescent, aerated, unbuffered 3.5 wt% NaCl solution with a pH of approximately 8.6. After completion of the 4-h OCP period, anodic potentiodynamic polarization was performed at a scan rate of 0.1 mV/s from the OCP to a potential +700 mV more positive than the OCP, whereas cathodic potentiodynamic polarization scans were performed from OCP to the potential of – 1.4 $V_{sat\ Ag/AgCl}$; scans were terminated if the measured current density exceeded 10 mA/cm^2. Ohmic resistance corrections were made to the polarization scans by determining ohmic resistance with electrochemical impedance spectroscopy. Each alloy was tested a minimum of three times for repeatability.

Characteristic polarization curves for each alloy are given in Fig. 15 where the potential is on the y-axis and the measured current density is on the x-axis with a logarithmic scale. The corrosion potentials for the alloys ranked Vibenite 350 > Vibenite 280 > Vibenite 150 > rolled homogeneous armor (RHA) steel from most to least noble. Alloy 350 was the only alloy that showed any degree of passivation, as noted by the increase in anodic Tafel slope indicated from B to C on the plot. The other alloys displayed low anodic Tafel slopes, all less than 100 mV/decade (dec). For the cathodic kinetics, all alloys were initially subject to the oxygen reduction reaction (ORR) following Eq. 1:

$$O_2 + 2H_2O + 4e^- = 4OH^- \quad (1)$$

Alloy 350 displayed a large linear region for ORR between potentials of approximately –0.35 $V_{sat\ Ag/AgCl}$ to –0.45 $V_{sat\ Ag/AgCl}$ before reaching the diffusion-limiting current density for ORR. All other alloys displayed small regions of ORR before reaching the diffusion-limiting current with possible cathodic corrosion indicated by the areas marked A in Fig. 15. Eventually, the primary cathodic reaction became dominated by the hydrogen evolution reaction (HER) indicated by the linear region from approximately –1 $V_{sat\ Ag/AgCl}$ to –1.4 $V_{sat\ Ag/AgCl}$ because HER is available as a possible cathodic reaction below –0.7064 $V_{sat\ Ag/AgCl}$: the HER is given by Eq. 2.

$$2H_2O + 2e^- = H_2 + 2OH^- \quad (2)$$

All Tafel parameters determined in this test are given in Table 9.

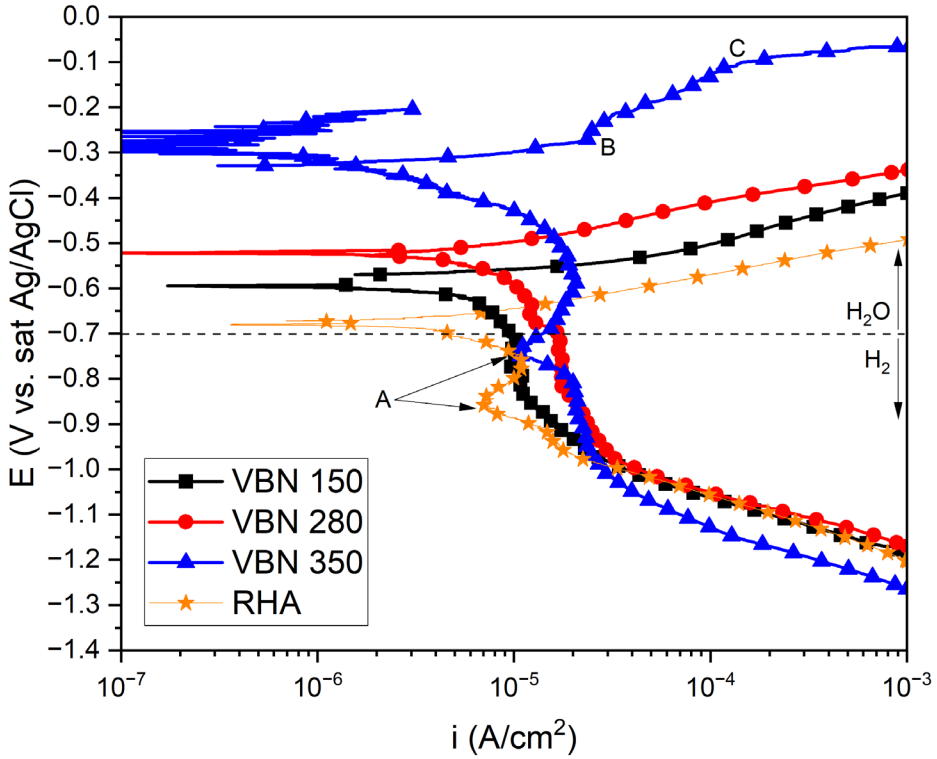

Fig. 15 Characteristic polarization curves in 3.5 wt% NaCl

Table 9 Tafel parameters extracted from potentiodynamic polarization curves

Alloy	ß$_a$ (mV/dec)	ß$_{c, ORR}$ (mV/dec)	I$_{lim}$ (A/cm^2)	ß$_{c, HER}$ (mV/dec)
150	85.7 ± 20.1	76.7 ± 14.1	8e-6 ± 9.4e-7	116.7 ± 2.5
280	95.0 ± 7.5	142.3 ± 32.3	1.7e-5 ± 5.6e-6	119.3 ± 7.5
350	202.7 ± 12.2	124.3 ± 8.7	1.8e-5 ± 3.3e-6	139.3 ± 11.8
RHA	75.5 ± 1.9	104 ± 5.0	1.1e-5 ± 9.9e-7	132 ± 4.1

The corrosion current density for each alloy was determined using the Stearn-Geary approach using Eq. 3:

$$i_{corr} = \frac{\beta_a \beta_c}{2.303 R_p(\beta_a + \beta_C)}, \quad (3)$$

where i_{corr} is the corrosion current density, β_a is the anodic Tafel slop, β_c is the cathodic Tafel slope for ORR, and R_p is the polarization resistance, which was determined by linear regression of the anodic and cathodic polarization curves ±5 mV from OCP on a linear E versus i plot. The resulting values for polarization resistance and corrosion rate are given in Table 10, where the corrosion rate of Alloy 150 was 9.3 times faster than RHA, Alloy 280 was 1.3 times faster than RHA, and Alloy 350 was 3 times slower than RHA. The results for Alloy 350 are not surprising given the high Cr content relative to the alloy tested, which typically aids in formation of a passive surface film resulting in improved corrosion protection.

Table 10 Measured polarization resistance and calculated corrosion current density for alloys tested in this study

Alloy	R_p(V/mA)	i_{corr}(A/cm^2)	i_{corr}vs. RHA
150	3.01	5.83 e-5	9.3×
280	3.08	8.02 e-6	1.3×
350	16.37	2.04 e-6	0.33×
RHA	3.03	6.28 e-6	…

4. Conclusions

This study has characterized a range of physical and mechanical properties for three steels produced via AM. Analytical microscopy indicated that all three alloys contained an appreciable amount of various micron-sized carbides. The presence of these carbides resulted in the steels having ultrahigh strengths and overall hardness but at the cost of a reduced level of tensile ductility. This observation was further confirmed in the wear and tensile results.

Based upon the various results, it was determined that the alloys lacked the required toughness (ductility) for use in high strain-rate and/or impact-related applications. Instead, the alloys showed significant promise in wear resistance applications. Indeed, Alloy Vibenite 280 was found to have similar overall properties (mechanical, wear resistance, and corrosion) as alloy AISI 52100 and thus could be a potential substitute for this alloy, with the noted benefit of being produced via current AM methods. This ability could enable the potential redesign of existing parts to save weight or improve performance by leveraging production features possible in AM methods that are not available in conventional metal-forming operations (such as rolling, extrusion, milling, etc.).

5. References

1. ASTM International. Standard practice for conducting force controlled constant amplitude axial fatigue tests of metallic materials (E466-15). ASTM International; 2015. doi 10.1520/E0466-15.
2. Chen W, Song B. Split Hopkinson (Kolsky) bar design, testing, and applications. Springer; 2011. doi 10.1007/978-1-4419-7982-7.

List of Symbols, Abbreviations, and Acronyms

3D	three-dimensional
AISI	American Iron and Steel Institute
AM	additive manufacturing
ASTM	American Society for Testing and Materials
CT	computed tomography
dec	decade
EBSD	electron back-scatter diffraction
HER	hydrogen evolution reaction
OCP	open circuit potential
ORR	oxygen reduction reaction
RHA steel	rolled homogeneous armor steel
S-N	stress amplitude–cycles to failure

1 (PDF)	DEFENSE TECHNICAL INFORMATION CTR DTIC OCA
1 (PDF)	DEVCOM ARL FCDD RLB CI TECH LIB
8 (PDF)	DEVCOM ARL FCDD RLA MB J LIGDA P MOY B POWERS T WALTER FCDD RLA MF V HAMMOND T CAIN FCDD RLA VA N MURTHY M FERRERA